Research on Chemical Intermediates (2023) 49:4367–4382
https://doi.org/10.1007/s11164-023-05107-2

Catalytic performances of VPO/SBA-15 catalysts for ammoxidation of dichlorotoluenes

Dongmei Zhao[1] · Wanjun Tang[1] · Qingliang You[2] · Tingcheng Li[1] · Lang Sun[1] · Guangyong Xie[1]

Received: 18 April 2023 / Accepted: 4 August 2023 / Published online: 21 August 2023
© The Author(s), under exclusive licence to Springer Nature B.V. 2023

Abstract

Vanadium phosphorus oxide (VPO) was immobilized on SBA-15 via a facile impregnation process. The structure and VPO species on SBA-15 were characterized by XRD, TEM, BET, FTIR and XPS techniques. It was found the VPO/SBA-15 catalysts maintained the two-dimensional hexagonal structure of SBA-15, and the supported VPO species existed in a highly dispersed amorphous state. VPO/SBA-15 catalyst was tested for the ammoxidation of dichlorotoluenes (DCTs) to corresponding dichlorobenzonitriles (DCNs) in a lab-scale tube reactor. Compared with VPO/SiO_2 (large-pore silica-supported VPO), VPO/SBA-15 exhibited appreciable enhancement in the catalytic performance due to the unique channel structure of SBA-15. The yield and selectivity toward 2,4-DCN increased by 7% and 6%, while toward the sterically hindered 2,6-DCN increased by 7% and 13%, respectively.

Graphical abstract

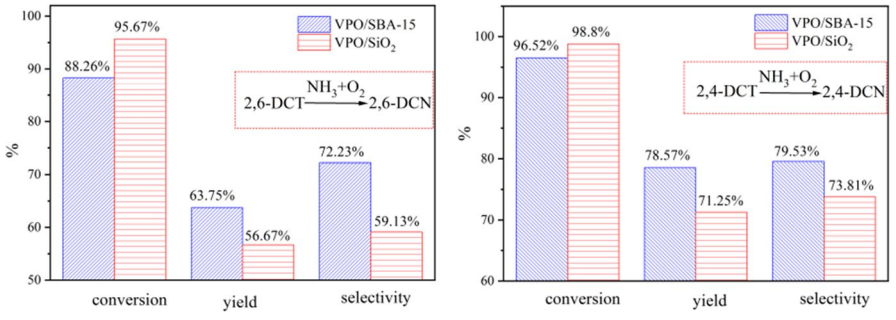

Keywords Ammoxidation · Mesoporous material · Catalyst · VPO · Dichlorobenzonitrile

Extended author information available on the last page of the article

Introduction

Aromatic nitriles, including chlorobenzonitriles, are very useful commodities and fine chemicals [1–3]. To avoid some toxic chemicals involved the production of aromatic nitriles on an industrial scale, catalytic ammoxidation of methyl aromatics and heteroaromatics has been explored as a preferred route [4–12]. Different types of catalysts have been developed during the last years. Comparing with V_2O_5, vanadium-based oxides exhibit improved catalytic performance and are preferentially used as bulk or supported catalysts for ammoxidation reactions [6–14]. Among them, VPO composite oxide catalysts, which are widely accepted that $(VO)_2P_2O_7$ is the major component [15], have attracted much attention due to their excellent catalytic performances in the reaction of C4 olefins to produce maleic anhydride [16, 17] and the partial oxidation of propane to produce acrylic acid [18, 19]. VPO is also widely used in the ammoxidation of aromatic hydrocarbons [20–22]. Supported VPO catalysts usually exhibit better behavior than unsupported ones in terms of mechanical properties, heat transfer capacity, and catalytic activity [23]. In order to understand the nature of the support, some common catalyst supports, such as SiO_2, TiO_2, Al_2O_3 and SiC have been studied as support materials for VPO [24, 25]. It was found that the nature of the support materials and the amount of VPO loading produced a profound effect on the physico-chemical characteristics of the dispersed VPO phase, leading to a marked change of the catalytic behavior.

Silica-based mesoporous molecular sieve materials with high surface area are widely used as supports for VPO catalysts. Nie et al. prepared a VPO catalyst supported on Al-modified MCM-41 molecular sieve [26, 27], which exhibited good catalytic effect in the partial oxidation of *n*-butane to maleic anhydride (MA). It is necessary for an ammoxidation catalyst carrier to have a high specific surface area to uniformly disperse the active component. A large pore size and volume is needed to promote the transfer of reactants and products. High diffusion and desorption rates are helpful for preventing deep oxidation of raw materials. However, for general catalyst carriers, the specific surface area and pore size are often mutually restricted. A high specific surface area often accompanies with a small pore size, which usually leads to the deposition of metal in the channels of the support and obstruction of the desorption and diffusion of the product, resulting in deep oxidation of the raw material and a low selectivity. In contrast, for a support with a large pore size and a small specific surface, low dispersion of the active component ensues and decreases the catalyst activity.

Although the pore size of MCM-41 is larger than that of microporous molecular sieves such as zeolite, its pore channels are still prone to be blocked in practical applications. Meanwhile, its pore walls are thin and the thermal stability is poor. SBA-15 mesoporous molecular sieve has a regular hexagonal structure and channel distribution along with a large channel diameter and thick wall structure [28]. SBA-15 also exhibits higher thermal stability than MCM-41. In addition, the ordered structure of SBA-15 is quite different from that of microporous molecular sieves. This feature allows many transition metal ions to be introduced

into the framework of SBA-15 and good long-term stability could be achieved by adopting SBA-15 as a support [24].

Due to its special structural properties, SBA-15 has been widely used in many fields. For example, SBA-15 was used as a template to synthesize ordered mesoporous carbon materials [29]. SBA-15 was modified with C_{18} as a packing material for chromatographic columns [30]. Chytil et al. [31] reported the impregnation of Pt, Ag, and Au in the pores of SBA-15. SBA-15 contains a large number of silanol groups on the surface, making it widely used in the field of catalysis [32–34]. Chemical grafting can be used to introduce species with catalytic activity to prepare supported catalysts and to improve the catalytic performance.

SBA-15 has also been extensively utilized as supports for fabricating highly dispersed VPO catalysts. Li et al. [35] supported VPO on SBA-15 and obtained fairly good catalytic activity for the oxidation of *n*-butane to maleic anhydride. VPO/SBA-15 catalysts also showed good performance for the partial oxidation of *n*-butane and propane [36]. Hu et al. [37] reported that VPO/SBA-15 catalysts exhibited high catalytic activities for the aldol condensation of acetic acid with formaldehyde to acrylic acid. Also, the catalytic performance of bulk and γ-Al_2O_3 supported VPOs have been tested for the ammoxidation of 2,6-dichlorotoluene [38]. However, there were very few reports on the catalytic aspects of SBA-15 supported VPO for the ammoxidation of dichlorotoluenes.

In the present work, SBA-15 was synthesized under hydrothermal conditions [28] and a 10 wt% SBA-15 supported vanadium-phosphorus composite oxide catalyst (VPO/SBA-15) was prepared by impregnation. The pore structure and composition were characterized with X-ray powder diffraction (XRD), transmission electron microscopy (TEM), infrared spectroscopy (FTIR), nitrogen physisorption and X-ray photoelectron spectroscopy (XPS). The catalytic performance of VPO/SBA-15 for the ammoxidation of 2,6-dichlorotoluene and 2,4-dichlorotoluene was evaluated.

Experimental

Catalyst synthesis

SBA-15 mesoporous materials were synthesized as follows. To a 500 mL single-necked flask, 10 g of P123 (Mn = 5800, from Aldrich) and 240 mL of dilute hydrochloric acid (2 mol/L) were sequentially added and heated in a water bath, and thoroughly stirred at 35 °C until P123 was completely dissolved. 23 mL of TEOS (ethyl orthosilicate) was added dropwise using a constant pressure dropping funnel. The mixture was stirred vigorously and the reaction was allowed to continue for 24 h. Then, the reaction mixture was poured into a crystallizing tank to crystallize at 100 °C for another 24 h. The resulting slurry was cooled to room temperature and suction-filtered. The precipitate was washed with distilled water for three times, and washed with ethyl alcohol for another three times, and dried at 60 °C overnight in an oven until the drying was complete. The white precursor obtained was placed in a muffle furnace and was sintered at 500 °C for 6 h to remove the templating agent.

At last, the products were naturally cooled and SBA-15 in white powder form was obtained.

The VPO/SBA-15 catalyst was prepared by an impregnation method. 2.57 g of $H_2C_2O_4{\cdot}2H_2O$ were dissolved in 80 °C distilled water. Then 1.565 g of 85% H_3PO_4 and 1.235 g of V_2O_5 were added. After stirring, a homogeneous dark blue solution was formed. 10.00 g of SBA-15 was accurately weighed in a beaker, and then the prepared dark blue hot liquid was poured into it. The mixture was stirred thoroughly, and then aged for 12 h. The aged catalyst was oven dried at 100 °C for 6 h to remove excess water, and then gradually heated to 500 °C at a rate of 5 °C/min in a muffle furnace. After activating via heating for 6 h, it was naturally cooled. VPO/SBA-15 catalyst with 10 wt% VPO content was obtained.

The VPO/SiO_2 catalyst was prepared via a similar procedure using the required quantity of silica gel (300–425 mesh).

Material characterization

X-ray powder diffraction (XRD) data was recorded by a Bruker D8 Advance X-ray powder diffractometer (Bruker, Germany) at 40 mA and 40 kV with Ni-filtered Cu-Kα radiation resource ($\lambda = 1.540598$ Å). The small 2θ angle changes from 0.5° to 5° at a scanning rate of 0.002° step per second, while large 2θ angle changes from 10° to 90°, at a scanning rate of 0.0163° step per second. For transmission electron microscopy (TEM) investigation, about 2 μL of alcohol suspension of VPO/SBA-15 was placed onto formvar/carbon film Cu grids (300 mess) and dried at ambient temperature. The TEM measurement was performed on a FEI Tecnai G^2 20 instrument (Dutch) operated at 200 kV. The pore structure parameters of the samples were measured on a Quantachrome Autosorb-1-C-TCD-MS instrument (Quantachrome Instrument, USA). Prior to the measurement, the samples were degassed and dried at 473 K for 4 h. N_2 adsorption/desorption isotherms were recorded at 77 K. The specific surface area was determined via the Brunauer–Emmett–Teller (BET) model. The total pore volumes and pore size distributions were determined from the N_2 adsorption data using the Barrett–Joyner–Halenda (BJH) method. XPS measurement was carried out using a MULT1LAB2000 X-ray photoelectron spectrometer (VG, USA). The binding energies were referenced to the C 1*s* peak at 284.5 eV. FTIR spectra were collected using a Nexus 470 FTIR spectrometer (Thermo Nicolet, USA) with the samples diluted in KBr.

Catalytic testing

The catalytic performance of prepared catalysts was evaluated in a fixed-bed tubular quartz micro-reactor. The bottom of the quartz tube was plugged with quartz wool. The SBA-15 and SiO_2 supported catalysts were diluted with ground quartz at a ratio of 1:3, and then put into the reactor. 2,6-dichlorotoluene (2,6-DCT) or 2,4-dichlorotoluene (2,4-DCT) was dosed using a micropump, vaporized and mixed in a preheating zone with NH_3 and air. The flow rates of NH_3 and air were respectively controlled using gas flowmeters. The product was collected for 8 h after the reaction

attained steady state conditions. The solid product was dissolved in ethanol and analyzed by a gas chromatograph.

The conversion of 2,6-DCT and 2,4-DCT, the yield and the selectivity of 2,6-dichlorobenzonitrile (2,6-DCN) and 2,4-dichlorobenzonitrile (2,4-DCN) were estimated as follows:

$$\text{Conversion rate} = \left(1 - \frac{\text{Amount of unreacted raw material}}{\text{Amount of raw materials entered}}\right) \times 100\%$$

$$\text{Molar yield} = \left(\frac{\text{Amount of product obtained}}{\text{Amount of due product}}\right) \times 100\%$$

$$\text{Selectivity} = \left(\frac{\text{Conversion rate}}{\text{Molar yield}}\right) \times 100\%$$

Results and discussion

X-ray powder diffraction (XRD)

The small-angle XRD patterns of SBA-15 and VPO/SBA-15 samples were given in Fig. 1. The XRD pattern of SBA-15 showed one strong peak at $2\theta = 0.9°$ and two weak peaks in the range of $1.5° < 2\theta < 2°$, corresponding to the (100), (110), and (200) planes, respectively, which were characteristics of the two-dimensional

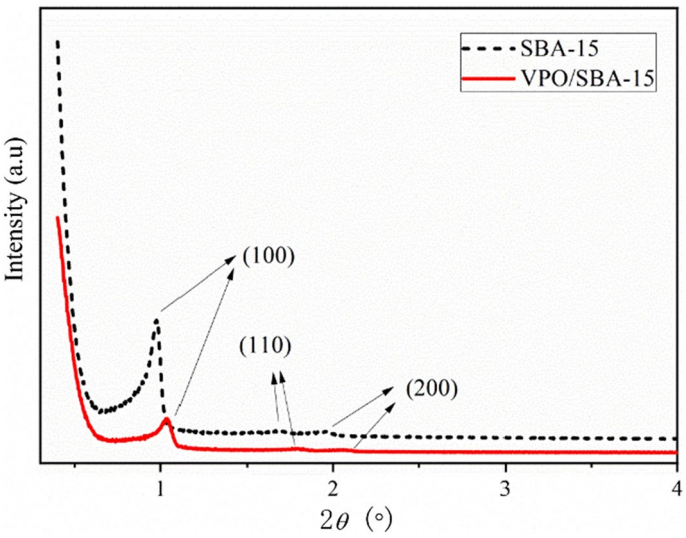

Fig. 1 XRD small-angle diffraction pattern of support and catalyst

hexagonal structure of SBA-15. The strong peak of (100) plane indicates that the pore structure was highly regular. The VPO/SBA-15 sample also exhibited three diffraction peaks assigned to the SBA-15 phase, suggesting that the long-range order of the SBA-15 framework was not dramatically changed after impregnation of VPO species. However, the XRD pattern of VPO/SBA-15 showed an obvious decrease in peak intensity, especially for (110) reflection. Meanwhile, the peak of (100) plane shifted to a high angle, suggesting that introduction of VPO species have partially shrunk the SBA-15 mesopores and reduced the long-range order of hexagonal channel microstructure [39, 40].

Figure 2 showed the wide-angle XRD patterns of SBA-15, VPO/SBA-15 and VPO/SiO_2 samples. At 10 wt% VPO loading for VPO/SBA-15 and VPO/SiO_2, all samples exhibited one broad diffraction peak at around 23° assigned to amorphous SiO_2. No diffraction peaks indicative of VPO crystallites were detected, suggesting that the VPO composite metal oxides supported on SBA-15 or SiO_2 were amorphous or highly dispersed [41].

Transmission electron microscope (TEM)

TEM images provides direct observation of the morphology and pore channel in SBA-15 and VPO/SBA-15. The high-magnification TEM image (Fig. 3a) showed a regular two-dimensional hexagonal channel structure, which is consistent with the SBA-15 structure that reported [28]. The TEM image of VPO/SBA-15 sample clearly revealed the highly ordered hexagonal channels of SBA-15, as shown in Fig. 3b. Bulk VPO crystallites were hardly distinguishable from the image, indicating that the VPO species were highly dispersed on the mesopore walls and were highly amorphous. This was consistent with the results of the large-angle XRD

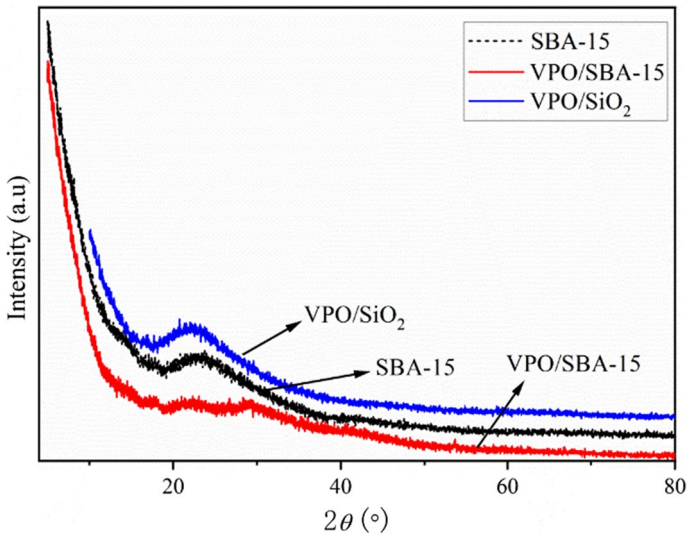

Fig. 2 XRD wide-angle diffraction pattern of support and catalyst

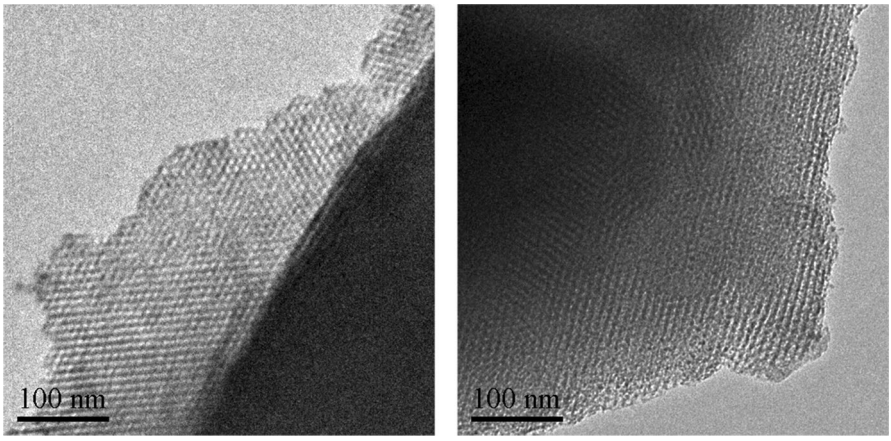

Fig. 3 TEM images of SBA-15 carrier (left) VPO/SBA-15 catalyst (right)

analysis. TEM images unambiguously confirm that the pore structure of SBA-15 was stable enough to support highly dispersed vanadium species.

Infrared spectrum (FTIR)

FTIR spectra of SBA-15 and VPO/SBA-15 samples were depicted in Fig. 4. A broad band peaked at 3460 cm^{-1} could be attributed to the stretching vibration of the terminal Si–OH and OH of physisorbed water on the surface of SBA-15. The band peaked at 1640 cm^{-1} was due to the bending vibration of the OH bond of water. The bands in the wavelength range of 400–1300 cm^{-1} were assigned to the stretching

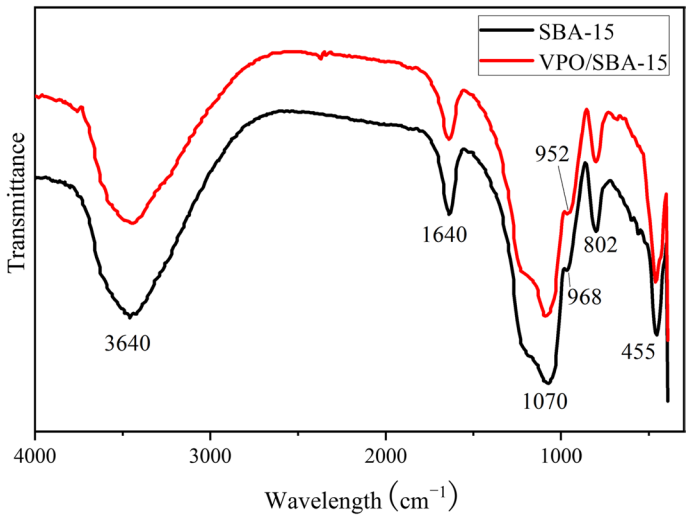

Fig. 4 FTIR spectra of SBA-15 support and VPO/SBA-15 catalyst

vibrations of the Si–O–Si bridges in the molecular sieve ring tetramer [42]. The bands at 455, 802, and 1070 cm^{-1} corresponded to the anti-symmetrical stretching vibration, symmetrical stretching vibration, and bending vibration of the Si–OSi bridges, respectively. By comparison, it could be seen that the three characteristic peaks attributed to the SBA-15 framework Si–O–Si were present in both the SBA-15 support and the VPO/SBA-15 catalyst, indicating that the introduction of VPO did not cause changes in its framework, and the catalyst still maintained the original structure of the carrier, which was consistent with the TEM results. The band at 952 cm^{-1}, which can be attributed to stretching vibrations of $V^{4+}=O$ species [43], provided the formation of $(VO)_2P_2O_7$ phase in the VPO/SBA-15 catalyst.

Nitrogen physical adsorption–desorption

In order to evaluate the change of surface areas and porosity of the SBA-15 support before and after VPO loading, N_2 adsorption–desorption was applied to SBA-15 and VPO/SBA-15 samples. The N_2 adsorption–desorption isotherms for SBA-15 support and 10 wt% VPO/SBA-15 sample were shown in Fig. 5. Both samples exhibited type IV isotherms and a typical hysteresis loop at a relative pressure (p/p_0) of 0.4–0.7, implying the presence of mesopores. The pore-size distribution curves of SBA-15 support and VPO/SBA-15 catalyst were presented in Fig. 6. Both SBA-15 support and VPO/SBA-15 exhibited uni-modal pore volume distribution with a dominant pore diameter around 4.15 nm, indicating that their pore structure was highly ordered. The BET surface areas of SBA-15 support and VPO/SBA-15 catalyst were listed in Table 1.

The SBA-15 support had a BET surface area of 746.7 m^2/g, while the BET surface area of VPO/SBA-15 catalyst was decreased to 302.1 m^2/g, along with the pore volume shifted from 0.67 to 0.39 cm^3/g. This was due to the penetration

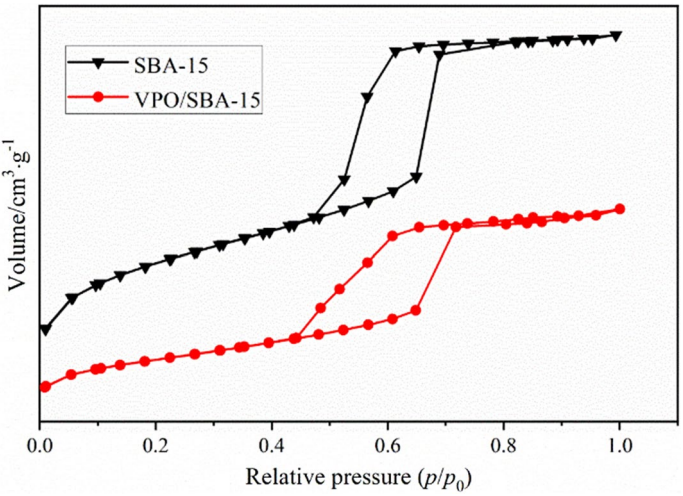

Fig. 5 N_2 adsorption–desorption curves of SBA-15 support and VPO/SBA-15 catalyst

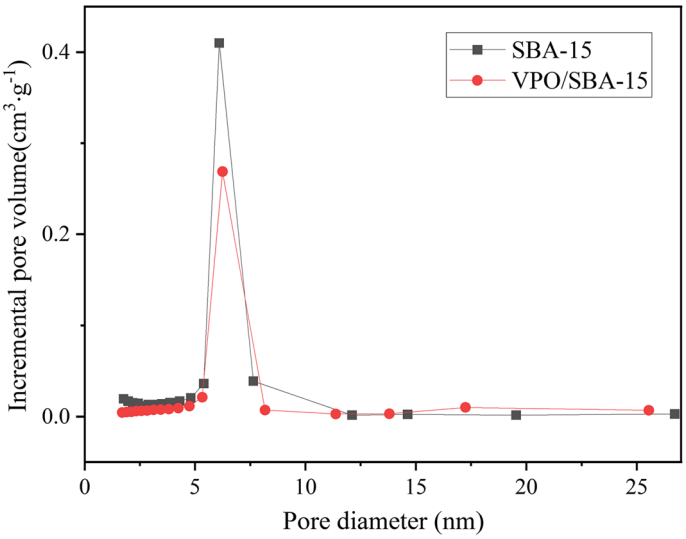

Fig. 6 Pore size distribution of SBA-15 support and VPO/SBA-15 catalyst

Table 1 Pore structure parameters of support and catalyst

Sample	Specific surface (m^2 g^{-1})	Average pore size (nm)	Pore volume (cm^3 g^{-1})
SBA-15	746.7	4.11	0.67
VPO/SBA-15	302.1	4.15	0.39
VPO/SiO_2	217.2	8.91	0.48

of dispersed VPO species into the pores of SBA-15 [44], resulting in a decrease in both the surface area and the pore volume, although the framework was not destroyed and VPO introduced did not block the channel. This was beneficial for the diffusion and transfer of raw materials and products in the catalyst pores, resulting high selectivity of the catalyst. The specific surface area and pore diameter of VPO/SiO_2 were also listed in Table 1. The data show that the specific surface area of VPO/SiO_2 was only 217 m^2 g^{-1}. In comparison, the VPO/SBA-15 catalyst has a large improvement in specific surface area and pore structure, which provided favorable conditions for improving the catalytic performance.

Based on the above results, it could be deduced that the VPO composite oxide was successfully supported on the SBA-15 support, and the prepared VPO/SBA-15 catalyst had a highly ordered two-dimensional hexagonal mesoporous structure and a large surface area. The active species were highly dispersed on the catalyst surface and mainly existed in an amorphous form.

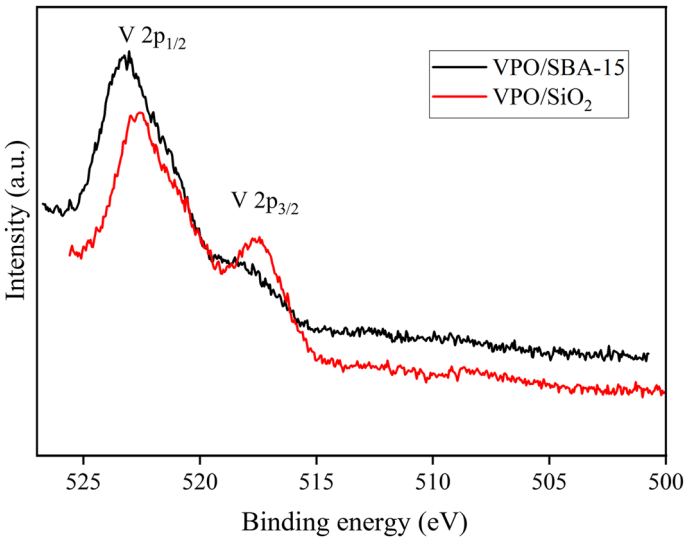

Fig. 7 Core-level spectra of V2*p* in the case of VPO/SBA-15 and VPO/SiO_2 catalysts

Table 2 Catalyst surface V and P atom ratios and electron binding energies of V2*p* and P2*p*

Catalyst	V $2p_{1/2}$ Electron binding energy(eV)	V $2p_{3/2}$ Electron binding energy(eV)	P 2*p* Electron binding energy(eV)	Surface P to V atomic ratio
VPO/SBA-15	523.05	517.70	134.91	9.00:1
VPO/SiO_2	522.67	517.17	134.28	7.79:1

X-ray photoelectron spectroscopy (XPS)

XPS analysis was performed to investigate the element valence and the enrichment of VPO oxides on the surface of SBA-15 support. High-resolution XPS spectra for the V2*p* core level of the studied VPO/SBA-15 and VPO/SiO_2 catalysts are shown in Fig. 7. The V and P ratios calculated from the V2*p* and P2*p* spectra were shown in Table 2. The binding energies at 523.05 and 517.70 eV were assigned to V$2p_{1/2}$ and V$2p_{3/2}$, respectively, which were the characteristic of V in the + 4 oxidation state [45]. This indicated that the vanadium species in the catalysts of VPO/SBA-15 and VPO/SiO_2 were mainly tetravalent.

In addition, XPS spectra showed an obvious phosphorus enrichment on the near-surface regions of VPO/SBA-15 and VPO/SiO_2 catalysts. The P/V atomic ratio on the surface of VPO/SiO_2 was about 7.79:1, while on the surface of the VPO/SBA-15 catalyst was about 9.00:1. Both were much larger than the normal P/V atomic ratio of 1:1. The surface enrichment of phosphor in the near-surface region might be contributed to the enhancement in the catalytic performance of VPO/SBA-15 [38].

Evaluation of ammoxidation activity

The catalytic behavior of the as-prepared VPO/SBA-15 catalyst was studied in the ammoxidation of 2,6-DCT and 2,4-DCT at atmospheric pressure, a space velocity (GHSV) of 590 h^{-1}, and a DCT:NH_3:Air ratio of 1:8:30. The ammoxidation reaction of 2,6-DCT over the VPO/SBA-15 catalyst was performed in the temperature range of 380–420 °C. According to the results (Fig. 8a), the conversion of 2,6-DCT increased significantly with increasing the reaction temperature. The yield and selectivity toward 2,6-DCN increased increasing temperatures up to 410 °C, and then decreased due to the further oxidation of 2,6-DCN. The ammoxidation of 2,6-DCT

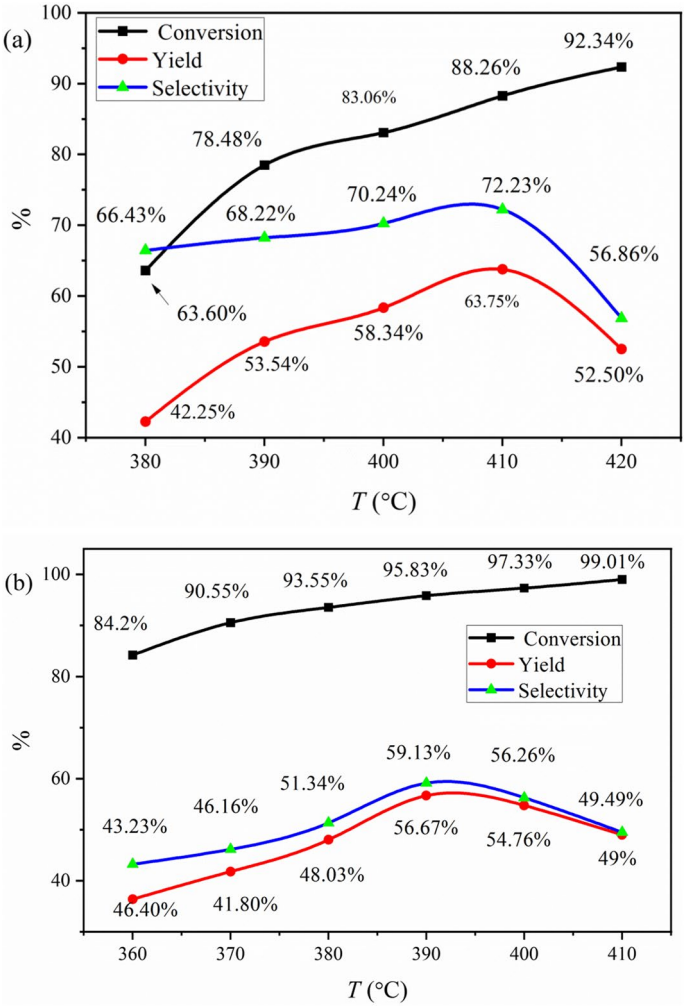

Fig. 8 Influence of temperature on conversion, yield and selectivity of 2,6-DCT (**a**: VPO/SBA-15; **b:** VPO /SiO_2)

over the VPO/SiO_2 catalyst was carried out in the temperature range of 360–410 °C and the results were presented in Fig. 8b. The reaction temperature of 390 °C gave the highest yield and selectivity. The conversion, selectivity and yield for the VPO/SiO_2 catalyst with increasing the reaction temperature followed a similar trend. The VPO/SBA-15 catalyst displays much better catalytic performance in comparison to VPO/SiO_2 catalyst. Under optimal reaction temperature at 410 °C, the VPO/SBA-15 catalyst gave the best yield (63.75%) and selectivity (72.23%) for 2,6-DCN with 88.26% conversion of 2,6-DCT.

Under the same test conditions, the conversion, yield and selectivity toward 2,4-dichlorobenzonitrile (2,4-DCN) as a function of temperature over VPO/SBA-15 and VPO/SiO_2 catalysts were shown in Fig. 9, with the optimal temperatures found at 410 and 370 °C, respectively. The best yield and selectivity of 2,4-DCN obtained over the VPO/SBA-15 catalyst reached up to 78.57% and 79.53% with a conversion of 98.8%, while the VPO/SiO_2 catalyst exhibited a maximum 2,4-DCN yield of 71.25% at a conversion of 96.53%.

The above results indicated that VPO/SBA-15 was an effective catalyst for the ammoxidation of chlorotoluenes. Figure 10 showed the catalytic performances of VPO/SBA-15 and VPO/SiO_2. VPO/SBA-15 gave appreciable chlorobenzonitrile selectivity of 70%. Especially, the selectivity toward 2,6-DCN was more than 80%. VPO/SiO_2 was superior to VPO/SBA-15 in terms of activity, whereas the yield and selectivity of VPO/SBA-15 toward 2,6-DCN were increased by 7% and 13%, respectively.

The yield and selectivity toward 2,4-DCN were also increased by 7% and 6%, respectively. VPO/SBA-15 exhibited higher selectivity and yield, particularly for the conversion of 2,4-DCT. The high performance of VPO/SBA-15 catalyst could be ascribed to its high surface area and structural features. The VPO species were highly dispersed on the surface of SBA-15. High surface area of VPO/SBA-15 catalyst provided large numbers of surface active sites. Meanwhile, VPO/SBA-15 catalyst with well-ordered hexagonal arrays of mesopores offered a large space for the diffusion of aromatic products, which promoted its fast desorption from the catalyst surface, thereby keeping them away from deep oxidation. The pore diameter and channel structure regularity of SBA-15 facilitated the transfers of raw materials and the products and then improved the yield and selectivity.

As shown in Fig. 10, VPO/SBA-15 exhibited different catalytic performance for 2,4-DCT and 2,6-DCT due to the influence of steric hindrance. The two neighbouring bulky Cl atoms in 2,6-DCT led to a very difficult accessibility to the CH_3 group [46], while the 2 Cl atoms at 2- and 4-positions in 2,4-DCT are dispersed, making it easy to approach the CH_3 group. Thus, VPO/SBA-15 displayed better catalytic performance for the ammoxidation of 2,4-DCT.

Conclusions

In this study, VPO composite oxide supported on SBA-15 has been successfully synthesized by the impregnation method. Although the surface area decreased after loading VPO, the 2-dimensional hexagonal structure of SBA-15 was retained. The

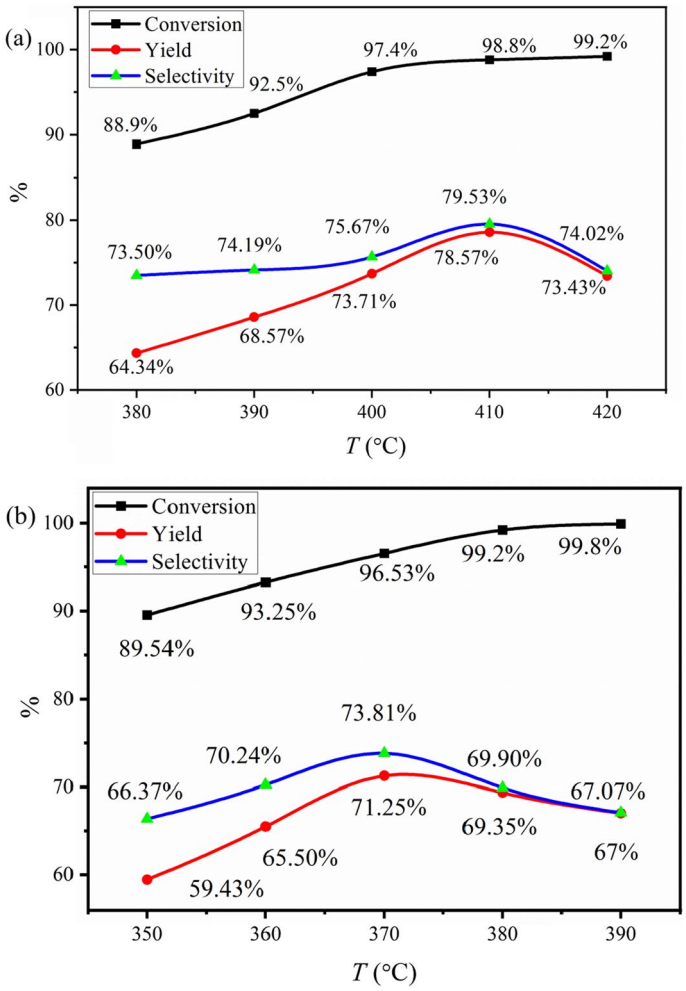

Fig. 9 Influence of temperature on conversion, yield and selectivity of 2,4-DCT (**a:** VPO/SBA-15; **b:** VPO/SiO_2)

VPO species were highly dispersed on the support in an amorphous state. The XPS results confirmed that a lower level of phosphorus enrichment occurred on the surface of VPO/SBA-15 than on VPO/SiO_2. The catalytic performance of VPO/SBA-15 catalyst was tested for the ammoxidation of 2,4- and 2,6-DCTs. Compared with VPO/SiO_2, VPO/SBA-15 exhibited lowered catalytic activity but improved yield and selectivity for DCNs. For 2,6-DCT with large steric hindrance, the advantage of VPO/SBA-15 catalyst was more pronounced.

Acknowledgements This work was supported by the National Natural Science Foundation of China (Grant No. 21172269), by "the Fundamental Research Funds for the Central Universities", South-Central Minzu University (Grant No. CZY22010), by "the Major bidding projects of provincial and ministerial

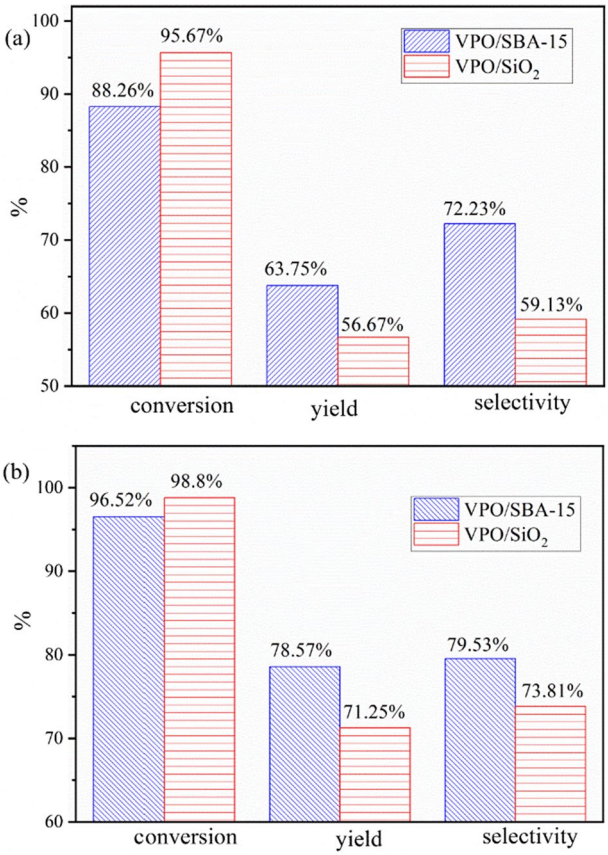

Fig. 10 Comparing the catalyst performance of VPO/SBA-15 and VPO/SiO_2 on the ammoxidation of 2,6-DCT (**a**) and 2,4-DCT (**b**)

scientific institutions", South-Central Minzu University (Grant No. PTZD22007), and by "the Opening Project of Key Laboratory of Optolectronic Chemical Materials and Devices of Minstry of Education", Jianghan Univeristy (Grant No. JDGD-202220).

Author contributions All authors contributed to the study conception and design. Material preparation, data collection, and analysis were performed by DZ and QY. The first draft of the manuscript was written by WT and LS. TL revised the manuscript, and all authors commented on previous versions of the manuscript. GX did project administration, supervised the work, revised, and completed the manuscript. All authors read and approved the final manuscript.

Funding Not applicable.

Data availability The data and materials can be accessed from the manuscript for the current study.

Declarations

Conflict of interest The authors declare that they have no known competing financial interests or personal relationships that could have appeared to influence the work reported in this paper.

Ethical approval Not applicable.

References

1. C. Janke, J. Radnik, U. Bentrup, A. Martin, A. Brückner, ACS Catal. **4**, 2687 (2014)
2. M. Ganesan, P. Nagaraaj, Org. Chem. Front. **7**, 3792 (2020)
3. H. Wang, D. Xu, E. Guan, L. Wang, J. Zhang, C. Wang, S. Wang, H. Xu, X. Meng, B. Yang, B.C. Gates, F.-S. Xiao, ACS Catal. **10**, 6299 (2020)
4. A. Martin, B. Lücke, Catal. Today **57**, 61 (2000)
5. Y. Goto, K. Shimizu, K. Kon, T. Toyao, T. Murayama, W. Ueda, J. Catal. **344**, 346 (2016)
6. W. Tang, H. Zheng, Y. Dong, Q. You, T. Li, G. Xie, Mol. Catal. **518**, 112062 (2022)
7. W. Tang, Y. Liu, S. Ding, Y. Dong, T. Li, G. Xie, Res. Chem. Intermed. **48**, 4105 (2022)
8. Y. Dong, T. Li, X. You, Q. You, L. Sun, G. Xie, Res. Chem. Intermed. **48**, 1151 (2022)
9. Y. Liu, D. Zhao, W. Tang, T. Li, Q. You, G. Xie, Hydrothermal synthesis of monoclinic CrVO4 nanoparticles and catalytic ammoxidation of 2-chlorotoluene. Catal. Lett. (2023). https://doi.org/10.1007/s10562-023-04305-2
10. Y. Huang, T. Li, Q. You, X. You, Q. Zhang, D. Zhang, G. Xie, Chin. J. Catal. **39**, 1814 (2018)
11. G. Xie, A. Zhang. Synth. Commun. **42**, 375 (2012)
12. G. Xie, A. Zhang, C. Huang, Res. Chem. Intermed. **36**, 969 (2010)
13. X. Li, C. Huang, Catal. Lett. **150**, 148 (2020)
14. B. Hari Babu, K.T. Venkateswara Rao, Y.W. Suh, P.S. Sai Prasad, N. Lingaiah, New J. Chem. **42**, 1892 (2018)
15. Y.E. Gorbunova, S.A. Linde, Soviet Phys. Doklady **24**, 138 (1979)
16. Y.H. Taufiq-Yap, Y.C. Wong, Y. Kamiya, W.J. Tang, J. Nat. Gas Chem. **17**, 232 (2008)
17. G.J. Hutchings, J. Mater. Chem. **19**, 1222 (2009)
18. G. Landi, L. Lisi, J.C. Volta, Chem. Comm. **4**, 492 (2003)
19. Y.-F. Han, H.-M. Wang, H. Cheng, J.-F. Deng, Chem. Comm. **6**, 521 (1999)
20. A. Martin, B. Lücke, Catal. Today **32**(1–4), 279 (1996)
21. M. Faizan, R. Zhang, R. Liu, J. Ind. Eng. Chem. **110**, 27 (2022)
22. N. Dropka, V.N. Kalevaru, A. Martin, D. Linke, B. Lücke, J. Catal. **240**, 8 (2006)
23. P. Borah, A. Ramesh, A. Datta, Catal. Commun. **12**, 110 (2010)
24. V.N. Kalevaru, B. Luecke, A. Martin, Stud. Surf. Sci. Catal. **175**, 393 (2010)
25. M.J. Ledoux, C. Crouzet, C. Pham-Huu, V. Turines, K. Kourtakis, P.L. Mills, J.J. Lerou, J. Catal. **203**, 495 (2001)
26. W. Nie, Z. Wang, W. Ji, Y. Chen, C.T. Au, Appl. Catal. A **244**(2), 265 (2003)
27. W. Nie, X. Wang, W. Ji, Q. Yan, C.T. Au, Catal. Lett. **76**(3), 201 (2001)
28. D. Zhao, J. Feng, Q. Huo, N. Melosh, G.D. Stucky, Science **279**(23), 548 (1998)
29. S. Jun, S.H. Joo, R. Ryoo, M. Kruk, M. Jaroniec, Z. Liu, T. Ohsuna, O. Terasaki, J. Am. Chem. Soc. **122**(43), 10712 (2000)
30. J. Zhao, F. Gao, Y. Fu, W. Jin, P. Yang, D. Zhao, Chem. Comm. **7**, 752 (2002)
31. S. Chytil, W.R. Glomm, E. Vollebekk, H. Bergem, J. Walmsley, J. SjBlom, E.A. Blekkan, Microporous Mesoporous Mater. **86**(1), 198 (2005)
32. R. Osuga, P. Fang, H. Nishiyama, K. Takizawa, N. Yagihashi, T. Yokoi, J.N. Kondo, Microporous Mesoporous Mater. **346**, 112278 (2022)
33. N. Deshpande, J.-Y. Chen, T. Kobayashi, E.H. Cho, H. Pineault, L.-C. Lin, N.A. Brunelli, J. Catal. **414**, 356 (2022)
34. P. Hongmanorom, J. Ashok, G. Zhang, Z. Bian, M.H. Wai, Y. Zeng, S. Xie, A. Borgna, S. Kawi, Appl. Catal. B **282**, 119564 (2021)
35. X.-K. Li, W.-J. Ji, J. Zhao, Z.-B. Zhang, C.-T. Au, J. Catal. **238**, 232 (2006)
36. X.-K. Li, W.-J. Ji, J. Zhao, Z. Zhang, C.-T. Au, Appl. Catal. A **306**, 8 (2006)
37. J. Hu, Z. Lu, H. Yin, W. Xue, A. Wang, L. Shen, S. Liu, J. Ind. Eng. Chem. **40**, 145 (2016)
38. V.N. Kalevaru, B. Lücke, A. Martin, Catal. Today **142**, 158 (2009)
39. Y.M. Liu, Y. Cao, N. Yi, W.L. Feng, W.L. Dai, S.R. Yan, H.Y. He, K.N. Fan, J. Catal. **224**, 417 (2004)
40. Y.M. Liu, Y. Cao, S.R. Yan, W.L. Dai, K.N. Fan, Catal. Lett. **88**, 61 (2003)

41. G. Du, S. Lim, M. Pinault, C. Wang, F. Fang, L. Pfefferle, G.L. Haller, J. Catal. **253**, 74 (2008)
42. L.M. Yang, Y.J. Wang, G.S. Luo, Y.Y. Dai, Microporous Mesoporous Mater. **81**(1), 107 (2005)
43. C. Santra, S. Shah, A. Mondal, J.K. Pandey, A.B. Panda, S. Maity, B. Chowdhury, Microporous Mesoporous Mater. **223**, 121 (2016)
44. G.C. Bond, S.F. Tahir, Appl. Catal. **71**(1), 1 (1991)
45. C. Niu, J. Qi, M. Tian, Ceram. Int. **48**, 6874 (2022)
46. X. Li, N. Guo, S. Yang, C. Huang, Mater. Chem. Phys. **272**, 124976 (2021)

Publisher's Note Springer Nature remains neutral with regard to jurisdictional claims in published maps and institutional affiliations.

Springer Nature or its licensor (e.g. a society or other partner) holds exclusive rights to this article under a publishing agreement with the author(s) or other rightsholder(s); author self-archiving of the accepted manuscript version of this article is solely governed by the terms of such publishing agreement and applicable law.

Authors and Affiliations

Dongmei Zhao[1] · Wanjun Tang[1] · Qingliang You[2] · Tingcheng Li[1] · Lang Sun[1] · Guangyong Xie[1]

✉ Wanjun Tang
tangmailbox@126.com

✉ Guangyong Xie
xiegy@scuec.edu.cn

[1] Key Laboratory of Catalysis and Energy Materials Chemistry of Ministry of Education and Hubei Key Laboratory of Catalysis and Materials Science, South-Central Minzu University, Wuhan 430074, China

[2] Key Laboratory of Optoelectronic Chemical Materials and Devices, Ministry of Education, School of Chemical and Environmental Engineering, Jianghan University, Wuhan 430056, China